Long and short term variability of the possible nascent planetary nebula IRAS 22568+6141: A late thermal pulse?

Roldán A. Cala[1], Luis F. Miranda[1], José F. Gómez[1], Christophe Morisset[2,3], Federico Soto[2], Pedro F. Guillén[4], and Roberto Vázquez[2]

[1] Instituto de Astrofísica de Andalucía IAA–CSIC, Glorieta de la Astronomía s/n, 18008, Granada, Spain
e-mail: `rcala@iaa.es`
[2] Instituto de Astronomía, Universidad Nacional Autónoma de México, Apdo. Postal 877, 22800 Ensenada, B.C., Mexico
[3] Instituto de Ciencias Físicas, Universidad Nacional Autónoma de México, Av. Universidad s/n, 62210 Cuernavaca, Morelos, Mexico
[4] Observatorio Astronómico Nacional, Instituto de Astronomía, Universidad Nacional Autónoma de México, Apdo. Postal 106, 22800 Ensenada, B.C., Mexico

ABSTRACT

IRAS 22568+6141 has been classified as a low-ionisation planetary nebula (PN) and presents non-thermal radio continuum emission, which could be a signature of nascent PNe. We present intermediate-resolution long-slit spectra obtained in 2021 and 2023, high-resolution long-slit spectra taken in 2023, and a light curve at the r filter between 1953 and 2019, that reveal changes in IRAS 22568+6141 with timescales of decades and a few years. The object underwent an energetic event around 1990 that suddenly increased its brightness which has been fading since then. A comparison with a published spectrum from 1988 shows an increase of the Hβ flux in 2021 by factor of $\simeq$6 and the [O III] emission lines that were absent in 1988. Between 2021 and 2023 the Hβ flux decreased by a factor of $\simeq$1.7, and the [O III] emission lines almost vanished. These results and the variability observed in other emission lines indicate that IRAS 22568+6141 is recombining and cooling down between 2021 and 2023, and probably since 2005, as suggested by archival radio continuum and mid-IR observations. The intermediate- and high-resolution spectra show that the excitation of the emission lines is dominated by shocks in 2021 and 2023, and, probably, also in 1988, which may be related to the non-thermal radio continuum emission from the object. Although the variability might be due to changes in the physical conditions in the shocks or in a nova-like eruption, it accommodates better to that expected from a late thermal pulse, which is further suggested by a comparison with other similar objects. New observations and monitoring in the coming years are crucial to corroborate the origin of the variability.

Key words. planetary nebulae: individual: IRAS 22568+6141 – stars: evolution – stars: winds and outflows – circumstellar matter – ISM: jets and outflows.

1. Introduction

Planetary nebulae (PNe) consist of circumstellar matter photoionised by hot central stars that evolve towards the cooling white dwarf phase. This ionised gas is the origin of most of the radiation from PNe. The emission at optical and infrared wavelengths is dominated by forbidden and recombination emission lines, while in the radio domain, the main emitting mechanism is bremsstrahlung (or free-free radiation) from free electrons in the plasma. This thermal continuum free-free radiation is characterised by a spectral index (α, where $S_\nu \propto \nu^\alpha$) ranging from +2 (optically thick regime at low frequencies) to -0.1 (optically thin regime at high frequencies; e.g. Aaquist & Kwok 1991) However, Suárez et al. (2015) showed that the young PN IRAS 15103−5754 presents non-thermal radio continuum emission, with $\alpha \simeq -0.54$, compatible with synchrotron radiation. Several other possible PNe also present some evidence of non-thermal emission (Cerrigone et al. 2011, 2017). The detection of non-thermal radio continuum emission in a PN could be an indication that it is at a nascent stage, since in more evolved PNe the free-free radiation would completely veil this non-thermal continuum emission.

IRAS 22568+6141 (PN G110.1+01.9, α(2000) =22h58m51.6s, δ(2000)= +61°57′43.5″; hereafter IRAS22568) could be one of such nascent PNe. The optical spectrum presented by García Lario et al. (1991) (hereafter GL+91) shows emission lines that are compatible with a low-excitation PN and is characterised by relatively prominent [N II] and absent [O III] emission lines. The reported radio continuum emission by Cerrigone et al. (2011, 2017) suggests a negative spectral index ($\alpha \simeq -0.35$) that has been confirmed by Gómez et al. (in preparation) with quasi-simultaneous observations at different frequencies. Fig. 1 presents the Hubble Space Telescope (*HST*) image of IRAS22568 in the F606W filter. The nebula is bipolar and extends over $\simeq 8$″ along the main axis oriented at position angle P.A.$\simeq -30°$. The bipolar lobes are separated by a dark lane of width $\simeq 0$″25, where no optical emission is observed and seems to be obscuring the central star. Radio continuum observations by Cerrigone et al. (2017) at 8.4 GHz resolve the two lobes and show emission from a central core between the lobes.

As part of a project to identify, confirm, and characterise new nascent PNe with non-thermal radio continuum emission, we obtained intermediate and high-resolution long-slit spectra of IRAS22568 at different epochs. In this paper we show that the
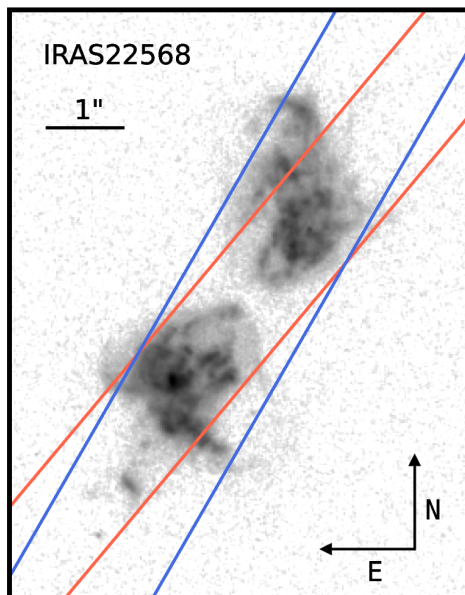
Fig. 1: *HST* (F606W) image of IRAS 22568+6141 with the long-slit position used for our spectra represented in blue (width = 2″, P.A. −30°), and the one used by GL+91 represented in red (width = 1″5, P.A. −40°).

source presents a peculiar variability in timescales of decades and a few years, as well as an internal kinematics not usually seen in PNe. The data presented here are crucial for understanding the nature of this possible nascent PN.

2. Observations and data reduction

2.1. Intermediate-resolution long-slit optical spectroscopy

We used the Calar Alto Faint Object Spectrograph (CAFOS) at the 2.2m telescope of the Calar Alto Observatory (Spain) on 2021 August 02 (proposal ID: F21-2.2-0.17; PI: R. A. Cala), and 2023 November 17 (proposal ID: DDT23B.320; PI: R. A. Cala) to obtain intermediate resolution long-slit spectra on IRAS22568. In Fig. 1 we show with blue lines the long-slit (width = 2″0) oriented at P.A. −30° along the major nebular axis. In both epochs the sky was photometric during the observations with a mean seeing of 2″1, and in both epochs we observed the standard star BD+28°4211 for flux calibration. The spectra were recorded in a SITe CCD with 2048×2048 pixel². The spatial scale in the detector is 0.53 arcsec pixel⁻¹. In 2021/2023 we obtained four/three spectra using grism B-100 (3200-6200 Å) with 1800 s exposure time each, and combined them into a single spectrum for each epoch. Also, in each epoch we obtained one spectrum with grism R-100 (5800-9600 Å) and 1800 s of exposure time. The spectra were calibrated following standard procedures in IRAF. We obtained a dispersion of ∼2 Å pixel⁻¹ after the wavelength calibration. PyNeb (version 1.1.19; Luridiana et al. 2015) was used to obtain the physical properties of the ionised gas, and Table A.1 lists the employed atomic constants.

2.2. High-resolution long-slit optical spectroscopy

High-resolution long-slit spectroscopy of IRAS 22568 was conducted on 2023 August 5–7 using the Manchester Echelle Spectrometer (MES) at the 2.1 m telescope on the San Pedro Mártir Observatory (Mexico) (proposal ID: FM-15; PI:

R. Vázquez). The long-slit (2″ width) was oriented at P.A. −30° (Fig. 1). The spectra were recorded in an E2V-4240 CCD with 1024×1024 pixel² and 4×4 binning, resulting in a spatial scale of 0″704 pixel⁻¹. Spectra of the Hα, [N II]λ6584, [S II]λ6730, and [O III]λ5007 emission lines (hereafter [N II], [S II], and [O III]) were obtained with exposure times of 1800, 1800, 3600, and 3600 s, respectively. A Th-Ar lamp spectrum was obtained immediately after each source spectrum for wavelength calibration. The spectra were reduced with IRAF. The average seeing during the observations was ∼1″8, and the spectral resolution is ∼11 km s⁻¹, as indicated by the full width at half maximum (FWHM) of the emission lines in the ThAr spectra.

3. Results

3.1. Spectral variability and physical properties of the ionised gas

Fig. 2 shows the intermediate-resolution spectra of IRAS22568 integrated over its two bipolar lobes. A simple look to our Fig. 2 and Fig. 3 in GL+91 reveals significant differences between the 1988, 2021, and 2023 spectra. Although our spectra resolve the two bipolar lobes of the object, for a better comparison between the spectra at the three epochs, we used the observed emission line fluxes in the integrated spectra for the analysis. The observed fluxes in 1988 can be found in GL+91 (their Table 2, column 3), and those in 2021 and 2023 are listed in Table B.1 .

We used the interstellar extinction law of Seaton (1979) to obtain the logarithmic extinction coefficient at Hβ, c(Hβ), and hereby, the intrinsic emission line intensities in the three epochs. The c(Hβ) was derived from the Hα and Hβ emission lines and a theoretical Hα/Hβ line intensity ratio of 2.85. We noticed that a similar c(Hβ) is obtained from the Paschen 9 (P 9) and Hβ emission lines, and a theoretical P 9/Hβ line intensity ratio of $18.4×10^{-3}$. The intrinsic line intensities, Hβ flux, and c(Hβ) at the three epochs are listed in Table 1. The differences between the intrinsic line intensities in 1988 obtained by us (listed in our Table 1, column 4) and those obtained by GL+91 (listed in their Table 2, column 4) are not significant and due to the different extinction law employed.

The most astonishing result is the presence in 2021 of the [O III] λ4363,4959,5007 emission lines in the nebula with I([O III])/I(Hβ)≃1.7, which were absent in 1988 (GL+91). Using the intensity of the weakest emission line detected in the spectrum from 1988 (I(P 10)/I(Hβ)≃0.016; Table 1) as an upper limit to the detection of the [O III] lines, they have emerged between 1988 and 2021 or, at least, their intensity has increased by more than two orders of magnitude in that time span. Further impressive is the subsequent variability of the [O III] λ4959,5007 emission lines whose intensity relative to Hβ has decreased by a factor of ≃3 between 2021 and 2023, while the [O III]λ4363 line is not detected in the last epoch.

More emission properties of the ionised gas have also substantially changed in IRAS22568. Table 1 shows that the Hβ flux increased by a factor ≃6 between 1988 and 2021. This value should be taken with some care considering that the long-slits used in 1988 and 2021 do not cover exactly the same regions of the object (Fig. 1), as well as the different extinction (see below) and sensitivity of the observations. However, a large increase of the Hβ flux between 1988 and 2021 should be considered real. Between 2021 and 2023 the Hβ flux decreased by a factor of ≃1.7 and we note that these two spectra were obtained under almost identical conditions (Sect. 2.1).
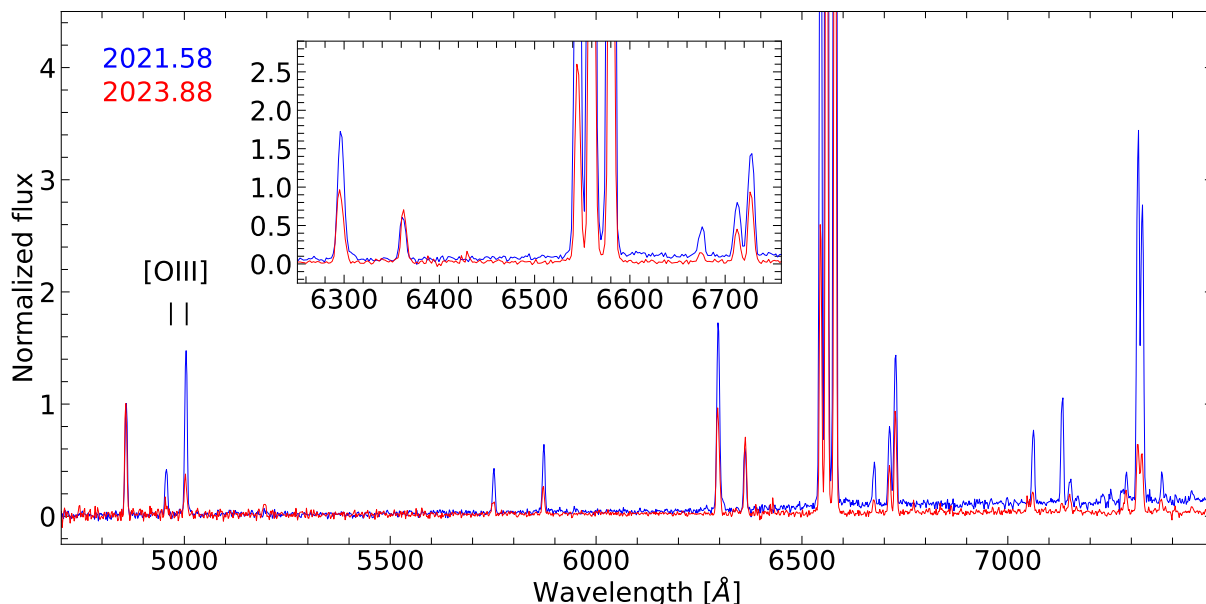
Fig. 2: Intermediate-resolution optical spectra of IRAS 22568+6141 obtained at the Calar Alto Observatory in 2021 (blue) and 2023 (red), normalized to peak flux of Hβ. The indicated [O III]λ4959,5007 emission lines were not detected in 1988 (see the text).

The value of c(Hβ) (Table 1) is decreasing since 1988 by factors of $\simeq$1.06 between 1988 and 2021, and $\simeq$1.8 between 2021 and 2023. Given that the nebular reddening E (B–V) and the nebular extinction Av are related by c(Hβ)=1.45$\times$E (B–V), and c(Hβ)=0.47$\times$Av (using the Seaton 1979, extinction law), we obtain Av(1988)=7.88$\pm$0.34 mag, Av(2021)=6.48$\pm$0.10 mag, and Av(2023)=3.53$\pm$0.10 mag. Therefore, the nebular extinction of IRAS22568 decreased 1.40$\pm$0.35 mag between 1988 and 2021, and 2.95$\pm$0.10 mag between 2021 and 2023.

Other emission lines present variability of their intensity relative to Hβ between 1988 and 2023. In the cases of very weak emission lines (e.g., Hγ, Hδ, [Cl II], and [Fe II]) that were not present in the 1988 spectrum, their detection in 2021 and/or 2023 may be due to a combination of increased nebular flux and better sensitivity in our spectra. In the cases of the [S II], [O I], [O II], and He I emission lines the variability can be considered real because these lines are relatively strong and detected in all three epochs. Moreover, an inspection of the 2021 and 2023 line intensities reveals that IRAS22568 has recombined in that time span. This is directly recognizable in (a) the decrease of the O^{2+}, O^+, and S^{2+} line intensities (relative to Hβ) in favour of those of O^+, O^0, and S^+, respectively, (b) the decreasing intensity of the Ar^{2+} emission lines, (c) the increasing intensity of the Fe^+ and Ni^+ ones, and (d) the decrease of the Balmer emission intensities. The [N II]λ6548,6583 emission lines present a slight increase in their relative intensities between 2021 and 2023 probably due to recombination from N^{2+} that proceeds faster than recombination from N^+ to N^0. Contrarily to that observed in the nebular [N II] lines, the auroral [N II]λ5755 line intensity clearly decreases between 2021 and 2023, implying that the nebula is also cooling down.

To calculate the electron temperature (T_e) we use the [N II](6584+6548)/5755 and [O II](4959+5007)/4363 emission lines ratios, while the electron density (N_e) was obtained from the [S II](6716/6731) line intensity ratio. These values were obtained making use of CROSSTEMDEN in PyNeb. The results are listed in Table 2. The values of T_e([N II]) are consistent with an increase of the excitation between 1988 and 2021,

and with cooling between 2021 and 2023. In 2021, when the [O II] λ4363 is detected, we obtained T_e([O III]) $\simeq$ 38400 K and T_e([N II]) $\simeq$ 17300 K. T_e([O III]) is anomalously high and very much higher than T_e([N II]). Such values can hardly be explained with photoionisation but clearly point out to shock excitation. This will be discussed in detail in Sect. 4.1. In 2023 we obtained an upper limit for the [O III] λ4363 line intensity (Table B.1), which does not allow us to derive T_e([O III]), while the [O III] lines were not detected in 1988.

As of the electron density (Table 2), the uncertainties in the line intensities in 1988 do not allow us to obtain an upper limit of N_e, suggesting that the nebula could have been in a high-density regime (see GL+91). On the other hand, the nominal values of N_e agree with each other within the errors. We noted that the values of N_e are averaged values integrated along the line of sight. The knotty structure of IRAS2258 suggests that N_e may present a relatively large range of values throughout the nebula (see e.g. Lee et al. 2022; Hyung et al. 2023).

With the values obtained for N_e (Table 2) we can estimate the recombination timescales assuming a recombination rate per ion $R_i \simeq 10^5$ yr $/(Z^2 N_e)$, where Z is the ionic charge (Osterbrock 1989). The recombination timescales of single and double ionised species result to be 8–12 and 2–3 yr, respectively, which are consistent with the fact that the [O III] emission lines have almost vanished between 2021 and 2023, while the Balmer ones show a more moderate decrease in intensity between those two epochs.

3.2. Light curve

In order to further investigate the optical variability of IRAS22568, we have searched for available photometric broadband *r*-filter observations in the literature and public surveys. We found six photometric values for the *r* magnitude from 1953 to 2020, that are reported in Table 3. However, the characteristics of the filters are not the same in the six epochs. The PanSTARRS filter is similar to that of GL+91, thus we transformed the magnitudes of SDSS to the PanSTARRS system magnitude (see Cham-

Table 1: Intrinsic line intensities ($I(\mathrm{H}\beta)=100$) in IRAS22568.

Emission line	$I(\lambda)$ 1988.58	$I(\lambda)$ 2021.58	$I(\lambda)$ 2023.88
4101 Hδ	$-^a$	40.71±2.16	$-^a$
4340 Hγ	$-^a$	57.12±3.72	$-^a$
4363 [O III]	$-^a$	8.81±2.29	$-^a$
4471 He I	$-^a$	7.6±0.7	$-^a$
4861 Hβ	100±10	100.0±1.6	100.0±2.5
4959 [O III]	$-^a$	40.70±1.15	15.02±1.60
5007 [O III]	$-^a$	119.09±1.35	40.58±2.01
5755 [N II]	8.05±0.79	11.00±0.28	7.65±0.30
5876 He I	11.73±1.11	13.83±0.25	12.86±0.40
6300 [O I]	25.89±1.32	22.25±0.19	67.16±0.68
6363 [O I]	10.03±0.49	8.10±0.18	26.88±0.64
6548 [N II]	73.9±1.3	70.04±2.46	80.33±1.67
6563 Hα	285.0±5.1	285.0±2.5	285.0±1.6
6584 [N II]	215.7±4.7	220.0±2.4	235.0±1.6
6678 He I	2.80±0.39	3.69±0.11	4.28±0.26
6716 [S II]	8.86±0.81	7.01±0.12	13.07±0.27
6731 [S II]	17.46±1.32	13.44±0.13	26.00±0.28
7002 O I	$-^a$	0.49±0.02	$-^a$
7065 He I	4.2±0.4	4.63±0.08	4.69±0.19
7137 [Ar III]	6.1±0.9	6.37±0.08	3.19±0.19
7150 [Fe II]	$-^a$	1.49±0.07	4.20±0.19
7230 [Fe II]	$-^a$	0.59±0.04	3.53±0.26
7254 O I	$-^a$	0.54±0.04	3.24±0.25
7281 He I	$-^a$	0.75±0.09	5.90±0.21
7319 [O II]	blended^b	19.98±0.15	15.16±0.22
7330 [O II]	blended^b	15.37±0.14	13.95±0.23
7378 [Ni II]	1.73±0.43	1.31±0.14	3.05±0.15
7447 [Fe II]	$-^a$	0.55±0.030	1.79±0.18
7751 [Ar III]	$-^a$	1.83±0.07	0.67±0.04
8446 O I	blended^c	3.33±0.06	1.61±0.11
8467 P 17	blended^c	0.81±0.05	0.71±0.04
8502 P 16	$-^a$	0.85±0.06	1.54±0.11
8545 P 15	$-^a$	1.09±0.06	1.97±0.14
8578 [Cl II]	$-^a$	0.77±0.06	2.26±0.12
8598 P 14	$-^a$	0.79±0.06	1.76±0.15
8605 [Fe II]	$-^a$	1.31±0.06	4.37±0.12
8665 P 13	$-^a$	1.27±0.06	2.26±0.14
8750 P 12	$-^a$	0.96±0.05	2.29±0.13
8863 P 11	$-^a$	1.53±0.05	2.71±0.11
8890 [Fe II]	$-^a$	0.91±0.05	2.29±0.11
9015 P 10	1.57±0.24	1.83±0.07	1.63±0.07
9069 [S III]	9.41±0.86	14.42±0.07	5.15±0.09
9229 P 9	3.45±0.43	3.44±0.08	5.10±0.15
9535 [S III]	22.34±1.52^d	32.22±0.19	11.86±0.30
$F(\mathrm{H}\beta)^e$	1.16±0.12	6.88±0.11	4.11±0.11
$c(\mathrm{H}\beta)$	3.70±0.16	3.05±0.05	1.66±0.04
A_V^f (mag)	7.88±0.34	6.48±0.10	3.53±0.09

Notes. ^{a} Not detected by GL+91 or in 2023.95. ^{b} [O II] $\lambda7319,7330$ are blended, with $I(\mathrm{sum})=32.63\pm2.26$. ^{c} O I $\lambda8446$ and P 17 $\lambda8467$ are blended with $I(\mathrm{sum})=6.09\pm0.61$. ^{d} Emission line blended with P 8 $\lambda9546$. ^{e} in units of 10^{-15} erg cm^{-2} s^{-1}. ^{f} Nebular extinction, see the text for details.

Table 2: Electron temperature and electron density of the ionised gas in IRAS 22568+6141 in the three epochs.

	1988.58^a	2021.58	2023.88
T_e [N II] (K)	13600±1000	17300±600	12400±300
T_e [O III] (K)	$-^b$	38400$^{+17000}_{-10500}$	$-^c$
N_e [S II] (cm^{-3})	12100$^+_{-8500}$	10600±2100	12900$^{+4500}_{-2900}$

Notes. ^{a} No reliable upper limit for the electron density could be obtained. ^{b} [O III] emission lines not detected. ^{c} [O III] $\lambda4363$ not detected.

Table 3: Multiepoch broadband *r*-filter photometry on IRAS22568.

Epoch	Survey^a	r (mag)	Reference
1953.8	POSS-I	16.16±0.25	Monet et al. (2003)
1990.5	–	16.7±0.3	GL+91
1991.7	POSS-II	15.15±0.25	Monet et al. (2003)
2003.7	SDSS	15.92±0.02	Avazajian et al. (2009)
2012.7	PanSTARRS	16.40±0.01	Chambers et al. (2019)
2019.5	ZTF	16.15±0.03	Masci et al. (2018)

Notes. ^{a} Palomar Observatory Sky Survey first (POSS-I) and second (POSS-II) release, Sloan Digital Sky Survey (SDSS), PanSTARRS survey, and Zwicky Transient Facility (ZTF) survey.
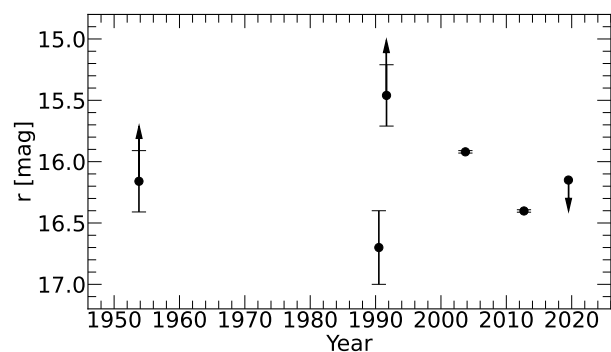
Fig. 3: Light curve of IRAS22568 in the *r*-filter. The arrows represent lower or upper limits. See the text for details.

be considered as upper limits to the *r* magnitude obtained in PanSTARRS.

Fig. 3 shows the *r* light curve of IRAS22568. Despite the limited temporal sampling and the lower/upper limits at some epochs, some trends can be seen. The *r* magnitude seems to have decreased ≥0.54 mag between 1953 and 1990.5, suddenly rose ≥1.5 mag between 1990.5 and 1991.7, and presented a steady decreasing tendency of ≥1 mag between 1991.7 and 2019.5. Our 2021 and 2023 spectra are consistent with this decrease (Table 1). Moreover, the flux density of the radio continuum emission has also been fading between 2005 and 2012 (Cerrigone et al. 2017).

3.3. Internal kinematics

Fig. 4 displays position-velocity (PV) maps of the Hα, [N II], [S II], and [O III] emission lines derived from the high-resolution long-slit MES spectra obtained in 2023.68, which are close in time to the intermediate resolution spectra from 2023.88. The MES spectra spatially resolve the NW and SE lobes of IRAS22568. The emission lines arise in two relatively compact

bers et al. 2019). The filter of ZTF is broader and has a transmission higher than the other filters, thus the magnitude from 2019.5 should be seen as a lower limit to the *r* magnitude measured in PanSTARRS. Finally, the POSS-I and POSS-II filters are narrower than the other filters, and their *r* magnitudes should
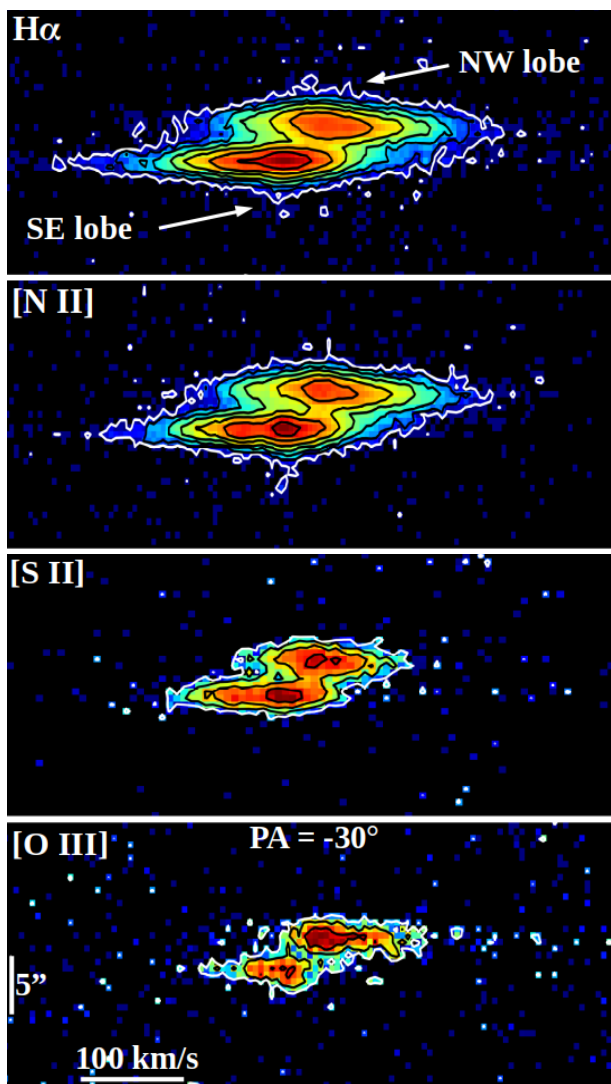
Fig. 4: Position-velocity maps of the Hα, [N ɪɪ], [S ɪɪ], and [O ɪɪɪ] emission lines obtained at a position angle P.A. −30 in 2023.68. The increment step of the contours is $3\sigma \times 2^n$, starting from $n = 0$ (white colour). The south-eastern lobe (SE lobe) and north-western lobe (NW lobe) are indicated.

Fig. 5: Normalized line profiles of the Hα, [N ɪɪ], [S ɪɪ], and [O ɪɪɪ] emission lines of the north-western (NW) and south-eastern (SE) lobes. The full-width at 10% the peak intensity (FW0.1) is shown as an horizontal dotted line.

regions and are characterised by a large velocity width that reach up to 450 and 380 km s^{-1} in Hα and [N ɪɪ], respectively, as measured at the 3σ level above the background (white contours in Figure 4). The [S ɪɪ] and [O ɪɪɪ] emissions are much fainter than the Hα and [N ɪɪ] ones, although they seem to present a similar profile. Fig. 5 presents the emission line profiles as obtained by integrating the emission of each lobe in a region of ≃2" centred on the emission peaks. Despite the differences in S/N, the [S ɪɪ] and [O ɪɪɪ] emission lines also exhibit large velocity widths that seem to be comparable to those observed in Hα and [N ɪɪ].

In Table 4 we list the spectral, spatial, and emission properties of NW and SE lobes derived from the PV maps (Fig. 4). We measured the radial velocity of the emission peaks (V_{peak}), the observed minimum (V_{min}) and maximum (V_{max}) radial velocities in the integrated spectra (see above) at the 10% level of the intensity peak (FW0.1) (which avoids the insertion of noise in the [S ɪɪ] and [O ɪɪɪ] emission lines, and allows us to obtain a coherent value from the four emission lines), the angular separation between the emission peaks of the two lobes, as obtained

from gaussian line fits to the spatial intensity distribution at the position of the intensity peaks, and the relative intensity of the emission peaks. Throughout this paper radial velocities will be quoted with respect to the Local Standard of Rest (LSR).

The emission peaks are separated by ≃37 km s^{-1}, the NW lobe being redshifted with respect to the SE one (Table 4). The centroid radial velocity of the two emission peaks is very similar in the four emission lines and their values are included in Table 4; their mean value is −93±1 km s^{-1} that will be considered the systemic velocity of the optical nebula. It is similar to, albeit somewhat larger than, the value of −85±2 km s^{-1} obtained by Sánchez-Contreras et al. (2012) from the CO emission, and the value of −80 km s^{-1} obtained by GL+91, perhaps due to the different spectral resolution. Secondary peaks are observed in the emission features, although more clearly in the SW lobe than in the NW one.

The FW0.1 in Hα and [N ɪɪ], amounts about 200 km s^{-1} in NW lobe and about 170 km s^{-1} in SE lobe. In [S ɪɪ] and [O ɪɪɪ], the values of FW0.1 are similar in both lobes and amount ≃173 and ≃147 km s^{-1}, respectively. It should be noted that the observed differences in FW0.1 are probably due to the different S/N ratio in the four emission lines.

The angular separation between the intensity peaks (Table 4) is different in each emission line. However, given the errors in the [S ɪɪ] and [O ɪɪɪ] emission lines, and that the line profiles of Hα and [N ɪɪ] are very well defined, the only conclusion is that the angular separation between Hα and [N ɪɪ] presents differences, while the separation in [S ɪɪ] and [O ɪɪɪ] seems to be similar to that of Hα. Finally, the SE lobe is stronger than the NW one in Hα and [N ɪɪ], the contrary is observed in [O ɪɪɪ], and both lobes present a similar intensity in [S ɪɪ] (Table 4).

4. Discussion

4.1. The shock-excited emission from IRAS22568

As already mentioned, the electron temperatures obtained in 2021 are incompatible with photoionisation and suggest shock excitation. In order to understand the origin of the line emission, we have made use of the Mexican Million Models Database (3MdB; Morisset et al. 2015), which allows us to analyse whether the line intensities are consistent with shocks or pho-

Table 4: Properties of the Hα, [N ɪɪ], [S ɪɪ], and [O ɪɪɪ] emission lines in the high resolution spectra.

| | NW lobe[a] | | | SE lobe[a] | | | | | |
Emission line	V_{peak}[b] km s^{-1}	V_{min}[c] km s^{-1}	V_{max}[c] km s^{-1}	V_{peak}[b] km s^{-1}	V_{min}[c] km s^{-1}	V_{max}[c] km s^{-1}	δR[d] "	V_{sys}[e] km s^{-1}	I_{NW}/I_{SE}[f]
Hα	-74 ± 1	-161 ± 2	$+36 \pm 2$	-112 ± 1	-216 ± 2	-43 ± 2	3.67 ± 0.04	-93 ± 1	∼0.44
[N ɪɪ]	-75 ± 1	-165 ± 2	$+27 \pm 2$	-112 ± 1	-212 ± 2	-49 ± 2	3.98 ± 0.04	-94 ± 1	∼0.49
[S ɪɪ]	-73 ± 2	-157 ± 2	$+13 \pm 4$	-107 ± 2	-222 ± 6	-46 ± 2	3.71 ± 0.11	-90 ± 1	∼0.82
[O ɪɪɪ]	-74 ± 2	-120 ± 2	$+28 \pm 3$	-113 ± 2	-200 ± 13	-54 ± 11	3.79 ± 0.12	-93 ± 1	∼1.19

Notes.[a] North-western lobe (NW lobe) and south-eastern Lobe (SE lobe) as indicated in Figure 4. Velocities are reported with respect to the LSR.[b] Velocity at the emission peak.[c] Minimum (V_{min}) and maximum (V_{max}) radial velocity at 10% ± 1σ of the peak, where σ is the noise of each PV map of Fig. 4.[d] Relative distance between the emission peaks of the two bow-shocks.[e] Systemic velocity, which is the mean value between the velocities at the emission peaks.[f] Relative intensity between the emission of the NW lobe (I_{NW}) and SE lobe (I_{SE}).

toionisation. In the Appendix C we explain the setup for the shock and photoionisation models employed below.

In Fig. 6 we show the location of shock and photoionisation models in a T_e–T_e diagram (namely, an [O ɪɪɪ]4363/5007 vs. [N ɪɪ]5755/6584 diagram) and the location of IRAS22568 in 2021 (red star). We do not try to look for the exact models that reproduce the observed line ratio, we rather use the maximum number of models to define the whole region where they are located in the T_e (O ɪɪɪ)–T_e(N ɪɪ) diagram, relative to the type of ionisation. While the [N ɪɪ]5755/6584 line intensity ratio can easily be reproduced by photoionisation and shock models, the high value of the [O ɪɪɪ]4363/5007 line intensity ratio can only be reproduced by shock models, the highest ratio obtained by photoionisation models still being 0.25 dex below the observed value.

If shocks were present in 2021, T_e cannot be determined in the classical manner and the values listed in Table 1 should be seen with caution. Determining T_e requires detailed models involving shocks (see e.g., Montoro-Molina et al. 2022), which are deferred to a future paper. We also noticed that if shock excitation exists, the Hα/Hβ theoretical ratio to determine c(Hβ) could be higher than the assumed value of 2.85. Thus, we have calculated c(Hβ) and intrinsic emission line intensities for an Hα/Hβ ratio of 3.1, but we obtained values that are very similar to and within the errors of those in Table 1.

The shocks observed in 2021 most probably are the mechanism responsible for the large velocity widths observed in the PV maps from 2023 (Fig. 4). In fact, emission lines with large velocity widths are well known in Herbig-Haro objects associated with young stars (e.g. Strom et al. 1974; Dopita 1978; Raga & Böhm 1986; Hartigan et al. 1987). Nowadays it is well established that this kind of emission features trace bow-shocks associated with high-velocity jets or bullets and their interaction with the surrounding medium.

Assuming the radiative bow-shock models by Hartigan et al. (1987), the shock velocity and viewing angle of NW lobe and SE lobe (Fig. 4) can be determined in a very simple way. We will concentrate in the Hα and [N ɪɪ] data that are of better quality, and note that the [S ɪɪ], and [O ɪɪɪ] data provide compatible results. The shock velocity is the difference between the observed V_{min} and V_{max} in Table 3. In the NW lobe the bow-shock velocity and viewing angle with respect to the observer are ≃195 km s^{-1} and ≃106±2° with respect to the line of sight, respectively; in the SE lobe the corresponding values are ≃170 km s^{-1} and ≃64±3°. Using the radial velocity of the intensity peaks (with respect to the systemic velocity) as representative of the velocity of the bow-
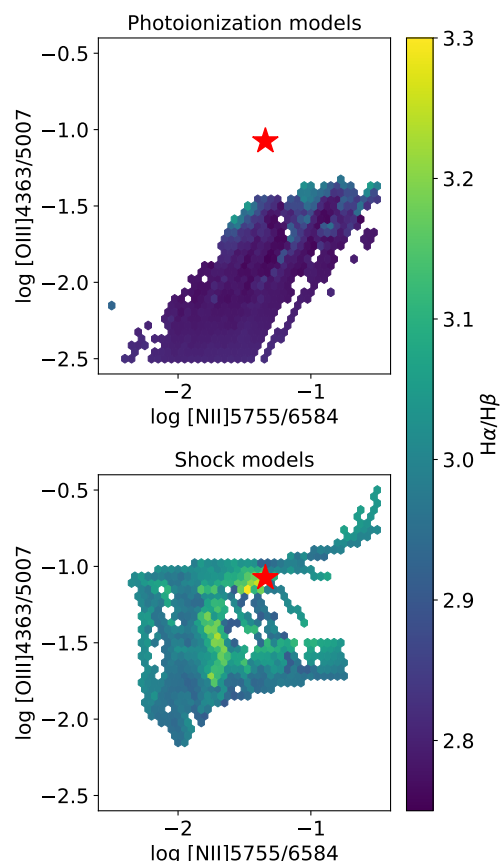
Fig. 6: Location of models from the 3MdB database (see text for details) in an [O ɪɪɪ]4363/5007 vs. [N ɪɪ]5755/6584 diagram. Top panel shows models of PNe, bottom panel shows shock and shock+precursor models. The color code for the models corresponds to the Hα/Hβ line intensity ratio. The red star is the location of the 2021 observations of IRAS22568.

shocks, we obtained velocities of ≃70 and ≃45 km s^{-1} in the NW and SE lobe, respectively.

We tried to identify which nebular features in the *HST* image (Fig. 1) could be associated with the bow-shocks, but IRAS22568 shows many knots and curved filaments, and, given the small angular size of the lobes, comparable to the spatial resolution of the MES spectra, it is difficult to pinpoint an association. On the other hand, we cannot rule out that the spectral features are an overlapping of several bow-shocks associated with

different knots and filaments in the bipolar lobes. If so, the viewing angle and expansion velocities obtained above may represent averaged values for each lobe, weighted by the contribution of each individual bow-shock. This may explain the differences in expansion velocity and tilt angle of each lobe without implying that the lobes have a different orientation.

A comparison of the Hα and [N II] PV maps shown in Fig. 4 with those by GL+91 (their Fig. 4) is revealing. Despite the differences in spatial and velocity resolution between both sets of PV maps, those by GL+91 show the emission peaks of each lobe, a secondary peak in the SE lobe, and a velocity width of ≃350–380 km s^{-1} at the spatial position of the intensity peaks, as measured at the weakest contour level. These results agree very well with ours, suggesting that bow-shock excitation could already be present in 1988. Moreover, our high-resolution spectra include a recombination (Hα), a high-excitation ([O III]), and two low-excitation ([N II] and [S II]) emission lines and, in all four cases, the emission features are compatible with bow-shock excitation. Therefore, it is possible that the optical spectrum of IRAS22568 in the three epochs is dominated by shocks. This raises doubts on the classification of IRAS22568 as a low-ionisation PN. Nevertheless, concluding that IRAS22568 is a post-AGB nebula could be premature because photoionised gas could be masked by shocks that are the dominant excitation mechanism. Furthermore, as an additional result, the existence of shocks might be intimately related with the non-thermal radio continuum emission from IRAS22568. Finally, it is worth to emphasize that, besides the T_e-sensitive line ratios in 2021 (Fig. 6), high resolution spatially resolved spectroscopy has been crucial to determine the excitation mechanism in 2023: without this kind of data, post-AGB nebula with shock-excited emission lines could be confused with low-ionisation young PNe, when observed at low- or intermediate-spectral resolution.

IRAS22568 belongs to a small group of post-AGB nebulae and PNe that present emission features with large velocity widths (typically ≥150 km s^{-1}) characteristics of bow-shock excitation. By means of high-resolution optical spectroscopy, large velocity widths have been detected in the PNe Hen 2-111 (Meaburn & Walsh 1989), M 1-16 (Schwarz 1992; Gómez-Muñoz et al. 2023), KjPn 8 (López et al. 1995), M 2-48 (Vázquez et al. 2000; López-Martín et al. 2002), and IRAS 18061−2505 (Miranda et al. 2021). Other PNe present bow-shaped structures that have been successfully reproduced using bow-shock models, although in these cases the structures do not exhibit such large velocity widths (typically 40–90 km s^{-1}) and they are irradiated by the central star; examples include K 4-47, IC 4634, and Hu 1-2 (Gonçalvez et al. 2004; Guerrero et al. 2008; Miranda et al. 2012; Fang et al. 2015, see also Mari et al. 2023 for more similar PNe). Similar emission features are observed in the post-AGB nebulae M 1-92 (Solf 1994), OH 231.8+04.2 (Sánchez-Contreras et al. 2000), Hen 3-1475 (Riera et al. 2003), M 2-56 (Sánchez-Contreras et al. 2010). The reason for the scarcity of large velocity widths associated with jets in PNe in not clear, although it could be related to photoionisation being the dominant excitation mechanism, which (partially) hides the shock-excited emission, and/or to a weakness of the shock contribution with time.

4.2. On the origin of the variability

The *r* light curve (Fig. 3) shows that IRAS22568 underwent an energetic event around 1990, which increased its brightness. The consequences of that event are perceptible until the present. The radio continuum emission from the nebula has been fad-
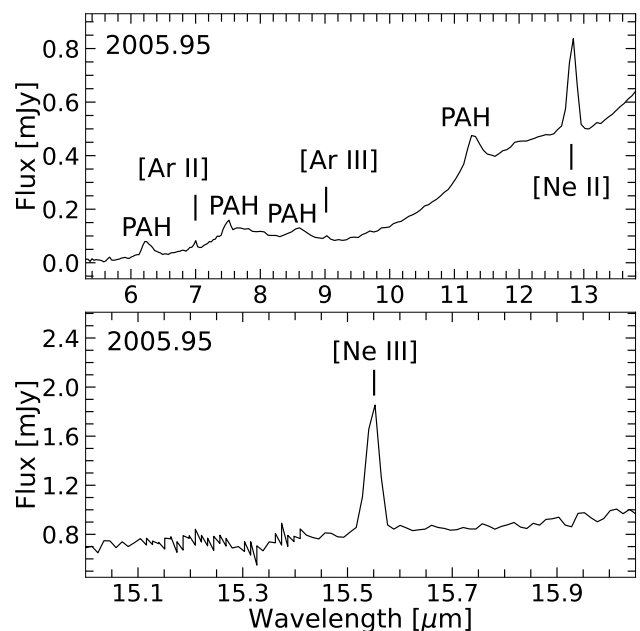
Fig. 7: *Spitzer* spectra of IRAS22568 obtained on 2005.95. Forbidden emission lines of ionised gas ([Ar II]$\lambda 7.0\mu m$, [Ar III]$\lambda 9.0\mu m$, [Ne II]$\lambda 12.8\mu m$, and [Ne III]$\lambda 15.55\mu m$) and broad emission of PAHs (6.4, 7.7, 8.6 and 11.3 μm) are indicated.

ing since at least 2005 (Cerrigone et al. 2017) and, according to our spectra, IRAS22568 is recombining and cooling down between 2021 and 2023. Moreover, we consulted the *Spitzer* Heritage Archive, and found spectra of IRAS22568 from 2005.95, which are shown in Fig. 7. These spectra display, among others, the [Ne III]15.6μm emission line which indicates that the nebular excitation was higher in 2006 than in later epochs (2021 and 2023) when the [O III] emission lines were relatively weak. Consequently, it is quite possible that the [O III] lines were stronger in 2006 than in 2021, and that IRAS22568 is recombining and cooling down since 2006 and even earlier. Finally, the spectral and kinematical properties provide clear evidence that the nebular emission is dominated by shocks in 2021 and 2023 and, perhaps, in 1988.

The variability of IRAS22568 could be due to changes of the physical conditions in the shocks. New ejections could have reached and interacted with the lobes by 1990. Similarly, already ejected material could encounter high density regions in the lobes and be decelerated by that date. In both cases, a rapid increase in T_e and N_e should be expected, resulting in an increase of the emission line fluxes and excitation. Once the interaction weakens or ceases, recombination and cooling down in the post-shock region would lead to a decrease in the excitation and brightness of the nebula, as observed since 2005-2006. Numerical simulations are necessary to check whether this scenario can account for the detailed observed variability and the involved time scales, and whether the physical conditions required for it to occur are reasonable for PNe. We note that, if the variability is due to changes in the shocks only, IRAS22568 would be a post-AGB nebula or proto-PN similar to, for example, M 1-92, rather than a PN.

Alternatively, a nova-like eruption could have been responsible for the sudden increase of brightness of IRAS22568. This kind of event is typical of binary systems hosting an AGB star and an accreting white dwarf. Such symbiotic binaries are in a different evolutionary phase than post-AGB stars and PNe. To

check whether IRAS 22568 could be related to this kind of binaries, we have built its spectral energy distribution (SED; see Appendix D) that is shown in Fig. D.1. The SED presents the emission peak at $\lambda \simeq 30\,\mu m$, which is typical of optically obscured post-AGB stars and young PNe (e.g. Ramos-Larios et al. 2009, 2012), but different from that of symbiotic binaries, where the peak of the SED usually lies at $\lambda \simeq 1\,\mu m$ (e.g. Rodríguez-Flores et al. 2014). Although more observations would be necessary, the SED of IRAS 22568 does not seem to favour a nova scenario as the cause of its variability.

Finally, a third possibility is a late-thermal pulse (LTP) occurred around 1990, as it is suggested by the remarkable similarities between the properties and temporal evolution of IRAS 22568 and those of the Stingray nebula (Hen 3-1357) whose central star, SAO 244567, has been proposed to undergo an LTP (Reindl et al. 2014, 2017). The light curves of IRAS 22568 (Fig. 3) and Hen 3-1357 (Schaefer et al. 2015) are similar to each other. In both objects, the spectral variability of the optical emission lines is consistent with cooling down and recombination during decades (see Sec. 3.1 and Arkhipova et al. 2013; Peña et al. 2022; Balick et al. 2021). Their radio continuum emission have been characterised by a fading of the flux density in the last decades, and negative spectral indices indicating non-thermal emission (Cerrigone et al. 2017; Harvey-Smith et al. 2018). As already mentioned, non-thermal emission and shocks appear related to each other in IRAS 22568 (Sect 4.1). The same may hold for Hen 3-1357 where shocks have been suggested to occur along the nebular perimeter (Balick et al. 2021). Similarly, a relationship between shocks and non-thermal radio continuum emission is observed after the (very late) thermal pulse occurred in Sakurai's object (Hajduk et al. 2024). Moreover, if an LTP in IRAS 22568 has generated a shock wave that propagates into the previous material, all the knots and filaments would be shocked, increasing the nebular brightness, excitation and the subsequent recombination and cooling down. Nevertheless, in the LTP scenario, the situation may be more complicated. The increase of the effective temperature of the central star after the LTP (Lawlor 2023, and references therein) would provide an additional source of ionising photons and the emission line spectra of IRAS 22568 would be produced in a combination of shocks and photoionisation, each presenting its own timescale of variability depending on the evolution of the central star and nebula. It is interesting to note that the *Spitzer* spectra (Fig. 7) display broad emission features attributed to dust made of polycyclic aromatic hydrocarbons (PAHs), which might be fresh byproducts of the LTP, and indicate carbon-rich material in the nebula. Finally, if the LTP scenario is correct, IRAS 22568 would indeed be a nascent PNe.

In contrast with SAO 244567 that is visible and its properties and evolution have been studied for decades (Henize 1976; Parthasarathy et al. 1993, 1995; Reindl et al. 2014, 2017), the central star of IRAS 22568 has never been observed and its current evolutionary stage is unknown. In particular, within the LTP scenario, we cannot assert whether the central star of IRAS 22568 is increasing its effective temperature or returning back to the AGB (see Hajduk et al. 2020). Millimeter observations could elucidate whether the molecular abundances of IRAS 22568 are similar to those in other sources in which an LTP seems to have occurred (e.g., Schmidt et al. 2018). In addition, a photometric and spectroscopic monitoring in the coming years and modelling of the data are key to trace the evolution of IRAS 22568 and confirm the origin of the variability.

5. Conclusions

IRAS 22568 has been classified as a low-ionisation PN and shows non-thermal radio continuum emission, suggesting to be a nascent PN. We performed on this source intermediate-resolution optical spectroscopy in 2021 and 2023, high-resolution spectroscopy in 2023, and gathered a discrete *r*-filter light curve from 1953 to 2020.

It is clear that an energetic event occurred in IRAS 22568 around 1990, which manifested itself as a sudden and rapid increase of the nebular brightness. Afterwards, the brightness has been diminishing much slower. As compared with a published spectrum from 1988, ours of 2021 shows a noticeable increase of the emission line fluxes and the presence of the [O III] emission lines which were not detected in 1988. Two years later, in 2023, the emission line fluxes decreased and the [O III] emission lines almost vanished. Actually, the observed spectral variability between 2021 and 2023 shows that IRAS 22568 is recombining and cooling down, a phenomenon that is probably occurring since at least 2005, as indicated by the reported fading of the radio continuum emission and archival mid-IR spectra around that epoch.

Some emission line ratios in 2021 reveal that the spectrum is shock-excited. Moreover, the large velocity widths ($\sim 400\,\mathrm{km\,s^{-1}}$) observed in the high-resolution 2023 spectra are compatible with bow-shock excitation, which could also be present in 1988. Our data suggest a connection between shock excitation and non-thermal radio continuum emission. Nevertheless, the existence of some contribution of photoionisation to the spectra cannot be discarded at least since 2006.

Changes of the physical conditions in the shocks could eventually explain the observed variability but modelling is necessary to confirm this scenario. A nova-like eruption would be another possibility, although this is not favored by the SED of IRAS 22568. Finally, a late thermal pulse in the central star of IRAS 22568 provides a simple and consistent explanation for the energetic event in 1990 and the subsequent photometric and spectral evolution of the object. In fact, we found noticeable similarities between the variability of IRAS 22568 and that of the Stingray nebula, which has been interpreted as due to a late thermal pulse.

References

Aaquist, O.B., & Kwok, S. 1991, ApJ, 378, 599
Alarie, A., & Morisset, C. 2019, Rev.Mex.Ast, 55, 377
Allen, A., M.G., Groves, B.A., Dopita, M.A., et al. 2008, ApJS, 178, 20
Arkhipova, V.P., Ikonnikova, N.P., Kniazev, A.Y., et al. 2013, Astron. Lett., 39, 201
Avazajian, K.N., Adelman-McCarthy, J.K., Agüeros, M.A. 2009, ApJS, 182, 543
Balick, B., Guerrero, M.A., & Ramos-Larios, G. 2021, ApJ, 907, 104
Chambers, K.C., Magnier, E.A., Metcalfe, N., et al. 2019, preprint (arXiv:1612.05560)
Cerrigone, L., Trigilio, C., Umana, G., et al. 2011, MNRAS, 412, 1137
Cerrigone, L., Umana, G., Triglio, C., et al., 2017, MNRAS, 468, 3450
Condon, J.J., Cotton, W.D., Greisen, E.W., et al. 1998, AJ, 115, 1693
Delgado-Inglada, G., Morisset, C. & Stasińska, G, 2014, MNRAS, 440, 536
Dopita, M.A. 1978, ApJS, 37, 117
Dopita, M.A., Sutherland, R.S., 1996, ApJS, 102, 161
Fang, X., Guerrero, M.A., Miranda, L.F., et al. 2015, MNRAS, 452, 2445
Ferland, G.J., Chatzikos, M., Guzmán, F., et al. 2017, Rev.Mex.Ast, 53, 385
Froese Fischer, C., & Tachiev, G., 2004, ADNDT, 87, 1
García Lario, P., Manchado, A., Riera, A., et al. 1991, A&A, 249, 223
Gonçalvez, D.R., Mampaso, A., Corradi, R.L.M., et al. 2004, MNRAS, 355, 37
Gómez-Muñoz, M.A., Vázquez, R, Sabin, L., et al. 2023, A&A, 676, 101
Guerrero, M.A., Miranda, L.F., Riera, A., et al. 2008, ApJ, 638, 272
Hajduk, M., Todt, H., Hamann, W.-R., et al. 2020, MNRAS, 498, 1205
Hajduk, M., van Hoof, P.AM., Zijlstra, A.A., et al. 2024, A&A, 688, L21
Hartigan, P., Raymond, J., & Hartmann, L, 1987, ApJ, 316, 323
Harvey-Smith, L., Hardwick, J.A., De Marco, O., et al. 2018, MNRAS, 479, 1842
Henize, K.G. 1976, ApJS, 30, 491
Hyung, S., Lee S.-J., & Otsuka, M. 2023, ApJS, 265, 2
Lawlor, T.M. 2023, MNRAS, 519, 5373
Lee S.-J., Hyung, S., Otsuka, M. 2022, ApJ, 938, 71
López, J.A., Vázquez, R., & Rodríguez, L.F. 1995, ApJL, 455, 63
López-Martín, L., López, J.A., Estaban, C., et al. 2002, A&A, 388, 652
Luridiana, V., Morisset, C., & Shaw, R.A. 2015, A&A, 573, 42
Mari, M.B., Gonçalvez, D.R., & Akras, S. 2023, MNRAS, 518, 3908
Marton, G., Gezer, I., Madarász, M., et al. 2024, A&A, 688, 203
Masci, F. J., Laher, R. R., Rusholme, B., et al. 2018, PASP, 131, 995
Meaburn, J., & Walsh, J.R. 1989, A&A, 223, 277
Miranda, L.F., Blanco, M., Guerrero, M.A., et al. 2012, MNRAS, 421, 1661
Miranda, L.F., Suárez, O., Olguín, L., et al. 2021, preprint (arXiv:2105.05186)
Monet, D.G., Levine, S.E., Canzian, B., et al., 2003, AJ, 125, 984
Montoro-Molina, B., Guerrero, M.A., Pérez-Díaz, B., et al. 2022, MNRAS, 512, 4003
Morisset, C., Delgado-Inglada, G., & Flores-Fajardo, N. 2015, Rev.Mex.Ast, 51, 101
Osterbrock, D.E., 1989, Astrophysics of Gaseous Nebulae and Active Galactic Nuclei. University Science Books, Herndon, VA
Parthasarathy, M., García-Lario, P., Pottasch, S.R., et al. 1993, A&A, 267, L19
Parthasarathy, M., García-Lario, P., de Martino, D., et al. 1995, A&A, 300, L25
Peña, M., Parthasarathy, M., Ruiz-Escobedo, F., et al. 2022, MNRAS, 515, 1459
Raga, A.C, & Böhm, K.H. 1986, ApJ, 308, 829
Ramos-Larios, G., Guerrero, M.A., Suárez, O., et al. 2009, A&A, 501, 1207
Ramos-Larios, G., Guerrero, M.A., Suárez, O., et al. 2012, A&A, 545, 20
Reindl, N., Rauch, T., Parthasarathy, M., et al. 2014, A&A, 565, 40
Reindl, N., Rauch, T., Miller Bertolami, et al. 2017, MNRAS, 464, L51
Riera, A., García-Lario, P., Manchado, A., 2003, A&A, 455, 203
Rynkun, P., Gaigalas, G., & Jönsson, P. 2019, A&A, 623, 155
Rodríguez-Flores, E.R., Corradi, R.L.M., Mampaso, A., et al. 2014, A&A, 567, 49
Sánchez-Contreras, C., Bujarrabal, V., Miranda, L.F., et al. 2000, A&A, 355, 1103
Sánchez-Contreras, C., Cortijo-Ferrero, C., Miranda, L.F., et al. 2010, ApJ, 203, 212
Sánchez-Contreras, C., & Sahai, R. 2012, ApJS, 203, 212
Schaefer, B.E., & Edwards, Z.I., 2015, ApJ, 812, 133
Schmidt, D., Woolf, N.J., Zega, T.J., et al. 2018, Nature, 564, 378
Schwarz, H., 1992, A&A, 264, L1
Seaton, M.J., 1979, MNRAS, 187, 73
Solf, J., 1994, A&A, 282, 567
Storey, P.J., & Zeippen, C.J., 2000, MNRAS, 312, 813
Storey, P.J., Sochi, T., & Badnell, N.R., 2014, MNRAS, 441, 3028
Strom, S.E., Grasdalen, G.L., & Strom, K.M., 1974, ApJ, 191, 111
Suárez, O., Gómez, J.F., Bendjoya, P., et al. 2015, ApJ, 806, 105
Sutherland, R.S., & Dopita, M.A., 2017, ApJS, 229, 34
Vázquez, R., López-Martín, R., Miranda, L.F., et al. 2000, A&A, 357, 1031
Tayal, S.S. 2011, ApJS, 195, 12
Tayal, S.S., & Zatsarinny, O. 2010, ApJS, 188, 32

Table A.1: Atomic data sets used for collisionally-excited lines in the PyNeb calculations.

Ion	Transition Probabilities[a]	Collision Strengths[b]
N^+	1	1
O^{2+}	1, 2	2, 3
S^+	3	3

Notes.[a] 1. Froese Fischer & Tachiev (2004). 2. Storey & Zeippen (2000) 3. Rynkun et al. (2019).[b] 1. Tayal (2011). 2. Froese Fischer & Tachiev (2004). 3. Storey et al. (2014). 4. Tayal & Zatsarinny (2010).

Appendix A: Atomic data sets used in PyNeb

Table A.1 shows the atomic data sets used for collisionally-excited lines in the PyNeb calculations presented in this paper.

Appendix B: Emission line fluxes of IRAS22568 in the three epochs.

In Table B.1 we report the emission line fluxes in 1988, 2021, and 2023. The emission line fluxes in 1988 are taken from GL+91 (their Table 2, column 4).

Appendix C: Parameters of the shock and photoionisation models in the 3MdB

Appendix C.1: Shock models

The shock models are taken from the work of Alarie & Morisset (2019) who computed models using Mappings V (Sutherland & Dopita 2017) and store them in the 3MdB (Alarie & Morisset 2019). These models use the same grid definition as Allen et al. (2008). We consider here the 15968 models that correspond to the "shock" and the "shock+precursor" results from the "Allen08" shock family, the precursor being the region photoionised by the photons emitted by the shock itself, for velocities higher than $100 \, \mathrm{km \, s^{-1}}$ (at lower velocities no ionising photons are produced by the shock). This preionisation is treated by Mappings in a fully consistent way and is described in detail by Sutherland & Dopita (2017). The free parameters of the grid are the metallicities, the pre-shock density, the shock velocity and the magnetic field. The details of the parameter distribution are given in Alarie & Morisset (2019).

Appendix C.2: Photoionisation models

The PN photoionisation models have been computed by Delgado-Inglada et al. (2014) using the multi-purpose transfer code CLOUDY v17 (Ferland et al. 2017). These models are taken from the 3MdB database, using the reference `ref LIKE "PNe_202_"`. We filter the models using the `com6=1 AND MassFrac > 0.7` commands. The first one is to only consider the realistic PNe models as defined in Sec. 2.1 of Delgado-Inglada et al. (2014) and in the grid model webpage[1]. The second filter is used to only select the radiation-bonded models, as well as the matter-bounded models in which the mass of the nebula is greater than 70% of the corresponding radiation-bounded case. The input parameters of the grid are: the nebular density and metallicity, the luminosity and effective temperature of the ionising spectral energy distribution (which can be a Planck function or a stellar atmosphere model), the presence or

[1] https://sites.google.com/site/mexicanmillionmodels
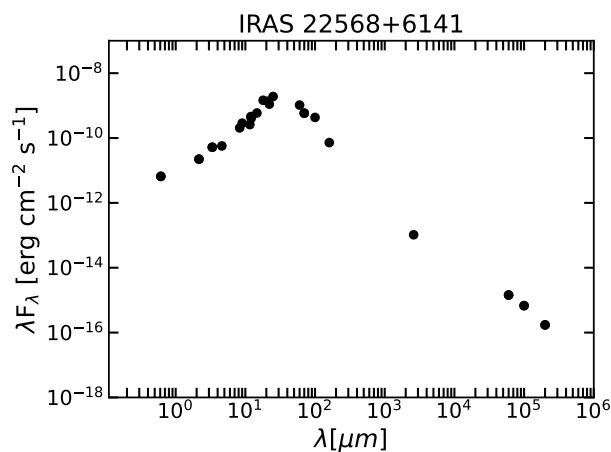
Fig. D.1: SED of IRAS22568. The size of the circles is larger than the errors.

absence of dust, the distance between the central ionising source and the inner radius of the nebula. This leads to 68041 models.

Appendix D: Spectral energy distribution (SED) of IRAS22568

We have gathered available archival optical, infrared, millimeter, and centimeter data (~ 0.5–$2 \times 10^5 \, \mu$m), and have built the SED of IRAS22568 (Fig. D.1). Infrared data were obtained from the Two Micron All Sky Survey (2MASS), AKARI, *Herschel* Space Observatory, Infrared Astronomical Satellite (IRAS), Midcourse Space Experiment (*MSX*), and Wide-field Infrared Survey Explorer (all-*WISE* survey). The flux density at 0.1 and 2.6 mm were taken from Marton et al. (2024) and Sánchez-Contreras et al. (2012), respectively. The flux density of the optical *r*-magnitude corresponds to the average value of those presented in the Table 3. Similarly, the radio flux density values are the average values reported by Cerrigone et al. (2017) at 4.8 and 8.6 GHz, while the value at 1.4 GHz was reported by Condon et al. (1998).

Table B.1: Absolute emission line fluxes F(λ) in units of 10^{-15} erg cm^{-2} s^{-1} on IRAS22568 in the three epochs.

Emission line	1988.58 F(λ)[a]	2021.58 F(λ)[a]	2023.88 F(λ)[a]
4101 Hδ	–	2.80±0.14	–
4340 Hγ	–	3.93±0.24	–
4363 [O III]	–	0.61±0.13	<34.4
4471 He I	–	0.52±0.04	–
4861 Hβ	1.16±0.11	6.88±0.11	4.11±0.11
4959 [O III]	–	2.80±0.08	0.62±0.06
5007 [O III]	–	8.19±0.09	1.67±0.08
5755 [N II]	0.48±0.04	0.757±0.019	0.314±0.012
5876 He I]	0.86±0.07	0.952±0.017	0.529±0.016
6300 [O I]	3.41±0.17	1.531±0.013	2.760±0.028
6363 [O I]	1.43±0.07	0.557±0.012	1.105±0.026
6548 [N II]	13.22±0.23	4.82±0.16	3.30±0.07
6563 Hα	51.9±0.9	19.61±0.17	11.71±0.07
6584 [N II]	40.3±0.9	15.14±0.16	9.66±0.07
6678 He I	0.58±0.07	0.254±0.007	0.176±0.010
6716 [S II]	1.91±0.16	0.482±0.008	0.537±0.011
6731 [S II]	3.84±0.27	0.925±0.009	1.069±0.011
7002 O II	–	0.034±0.0011	–
7065 He I	1.28±0.11	0.319±0.005	0.193±0.008
7137 [Ar III]	1.97±0.25	0.438±0.005	0.131±0.007
7150 [Fe II]	–	0.103±0.005	0.173±0.007
7230 [Fe II]	–	0.041±0.003	0.145±0.010
7254 O I	–	0.037±0.003	0.133±0.010
7281 He I	–	0.052±0.006	0.242±0.008
7319 [O II]	blended[b]	1.375±0.010	0.623±0.009
7330 [O II]	blended[b]	1.057±0.010	0.573±0.009
7378 [Ni II]	0.70±0.14	0.090±0.009	0.125±0.006
7447 [Fe II]	–	0.0383±0.0021	0.074±0.007
7751 [Ar III]	–	0.126±0.005	0.0280±0.0020
8446 O I	blended[c]	0.229±0.004	0.066±0.004
8467 P17	blended[c]	0.056±0.003	0.0294±0.0021
8502 P16	–	0.058±0.004	0.063±0.004
8545 P15	–	0.075±0.004	0.081±0.005
8578 [Cl II]	–	0.053±0.004	0.093±0.005
8598 P14	–	0.054±0.004	0.072±0.006
8605 [Fe II]	–	0.090±0.004	0.180±0.005
8665 P13	–	0.087±0.004	0.093±0.005
8750 P12	–	0.066±0.003	0.094±0.005
8863 P11	–	0.105±0.003	0.111±0.004
8890 [Fe II]	–	0.063±0.003	0.094±0.004
9015 P10	3.0±0.4	0.126±0.005	0.067±0.003
9069 [S III]	19.1±1.6	0.992±0.005	0.212±0.004
9229 P9	7.4±0.8	0.237±0.005	0.210±0.006
9535 [S III]	51.04±3.26[d]	2.217±0.013	0.487±0.012

Notes.[a] '–' stands for not detected.[b] [O II] λ7319,7330 are blended with F(sum)=12.6±0.8.[c] O I λ8446 and P 17 λ8467 are blended with F(sum)=5.8±0.5.[d] Blended with P 8 λ9546.